Published in final edited form as:
Matrix Biol. 2014 September ; 0: 48–58. doi:10.1016/j.matbio.2014.06.005.

WDR72 models of structure and function: A stage-specific regulator of enamel mineralization

K.A. Katsura, **J.A. Horst**, **D. Chandra**, **T.Q. Le**, **Y. Nakano**, **Y. Zhang**, **O.V. Horst**, **L. Zhu**, **M.H. Le**, and **P.K. DenBesten**
Department of Oral and Craniofacial Sciences, School of Dentistry, University of California, San Francisco, 513 Parnassus Ave., San Francisco, CA 94143-0422, USA

Abstract

Amelogenesis Imperfecta (AI) is a clinical diagnosis that encompasses a group of genetic mutations, each affecting processes involved in tooth enamel formation and thus, result in various enamel defects. The hypomaturation enamel phenotype has been described for mutations involved in the later stage of enamel formation, including *Klk4, Mmp20, C4orf26*, and *Wdr72*. Using a candidate gene approach we discovered a novel *Wdr72* human mutation in association with AI to be a 5-base pair deletion (c.806_810delGGCAG; p.G255VfsX294). To gain insight into the function of WDR72, we used computer modeling of the full-length human WDR72 protein structure and found that the predicted N-terminal sequence forms two beta-propeller folds with an alpha-solenoid tail at the C-terminus. This domain iteration is characteristic of vesicle coat proteins, such as beta′-COP, suggesting a role for WDR72 in the formation of membrane deformation complexes to regulate intracellular trafficking. Our *Wdr72* knockout mouse model (*Wdr72*$^{-/-}$), containing a *LacZ* reporter knock-in, exhibited hypomineralized enamel similar to the AI phenotype observed in humans with *Wdr72* mutations. MicroCT scans of *Wdr72*$^{-/-}$ mandibles affirmed the hypomineralized enamel phenotype occurring at the onset of the maturation stage. H&E staining revealed a shortened height phenotype in the *Wdr72*$^{-/-}$ ameloblasts with retained proteins in the enamel matrix during maturation stage. H^+/Cl^- exchange transporter 5 (CLC5), an early endosome acidifier, was co-localized with WDR72 in maturation-stage ameloblasts and decreased in *Wdr72*$^{-/-}$ maturation-stage ameloblasts. There were no obvious differences in RAB4A and LAMP1 immunostaining of *Wdr72*$^{-/-}$ mice as compared to wildtype controls. Moreover, *Wdr72*$^{-/-}$ ameloblasts had reduced amelogenin immunoreactivity, suggesting defects in amelogenin fragment resorption from the matrix. These data demonstrate that WDR72 has a major role in enamel mineralization, most notably during the maturation stage, and suggest a function involving endocytic vesicle trafficking, possibly in the removal of amelogenin proteins.

Correspondence to: P.K. DenBesten.
Appendix A. Supplementary data Supplementary data to this article can be found online at http://dx. doi.org/10.1016/j.matbio.2014.06.005.

Keywords

Amelogenesis imperfecta (AI); *Wdr72* knockout mouse; Hypomaturation; Vesicle trafficking; Protein modeling; Maturation-stage ameloblasts

1. Introduction

Amelogenesis Imperfecta (AI) is a genetically linked disease affecting tooth enamel development, varying in phenotype and inheritance pattern. Several genes encoding enamel matrix proteins and associated proteases, namely *Ambn* (MIM 601259), *AmelX* (MIM 300391), *Amtn* (MIM 610912), *Enam* (MIM 606585), *Klk4* (MIM 603767), and *Mmp20* (MIM 604629), were among the first identified candidate genes for AI (Hu et al., 2007; Wright et al., 2011). Recently, this list has grown with the advent of genome-wide searches and whole-exome sequencing, identifying *Fam20a* (MIM 611062) (Kantaputra et al., 2014; Wang et al., 2014), *Slc24a4* (MIM 609840) (Parry et al., 2013), and *C4orf26* (MIM 614829) (Parry et al., 2012). Also included in this list are *Fam83h* (MIM 611927) (Ding et al., 2009) and *Wdr72* (MIM 613214) (El-Sayed et al., 2009; Lee et al., 2010), which are thought to have vesicle-related functions in the enamel-producing ameloblasts, though their specific functions in vesicle trafficking remain unknown.

Six mutations in the *Wdr72* gene have been previously identified in humans affected with AI, all displaying hypomineralized enamel phenotypes in which the unerupted tooth enamel forms a matrix of normal thickness, but is radiolucent and abrades easily from the underlying dentin upon tooth eruption (El-Sayed et al., 2009; Lee et al., 2010; El-Sayed et al., 2011; Wright et al., 2011; Kuechler et al., 2012). This describes a hypomaturation defect, suggesting WDR72 function occurs during the maturation stage of enamel formation. Indeed, a previous study showed WDR72 to be expressed in murine ameloblasts with an increased expression during maturation stage (El-Sayed et al., 2009); however, the specific temporal and spatial expression of WDR72 during enamel maturation has not been characterized.

No other syndromic effects have been reported in AI patients carrying a *Wdr72* mutation, though one variant was reported to be associated with developmental problems in height, speech, respiration, and vision (Kuechler et al., 2012). Independent of AI, several *Wdr72* single nucleotide polymorphisms (SNPs) have been associated with kidney, heart, pancreatic, and neural diseases (Vasan et al., 2007; Kottgen et al., 2010; Paterson et al., 2010; Hertel et al., 2011; LeBlanc et al., 2012; Franceschini et al., 2014). Therefore, elucidating WDR72 function is of great importance for understanding mechanisms for tooth enamel mineralization and potential risk factors for disease in patients carrying a *Wdr72* mutation.

The function of WDR72 has been proposed to be vesicle-related, based on the known vesicle trafficking functions of WDR72's closest human homologue, WDR7 (El-Sayed et al., 2009; Lee et al., 2010). Both WDR72 and WDR7 are members of the WD40-repeat domain super family. Proteins in the WD40-repeat domain superfamily are defined by 4–8 repeating units of approximately 44–60 amino acids ending in tryptophan (W) and aspartic acid (D).

WD40 proteins typically contain several repeat domains that encode a series of anti-parallel β-sheet blades that configure into a well-stabilized, non-catalytic propeller, called a "β-propeller", for multi-unit complex docking (Stirnimann et al., 2010; Xu and Min, 2011). Proteins containing these β-propellers are observed in a broad range of cell processes, including signal transduction, cell cycle regulation, and vesicular trafficking; as such, they often contain other domain types that dictate specificities of function and pathway (Good et al., 2011). Our molecular modeling of WDR72 predicted a vesicle coat function, based on its conserved iteration of sub-structural domains and structural homology to β′-COP, a known protein structure that is a necessary component of the COPI vesicle coatomer.

To further investigate the function of WDR72 in enamel formation, we generated a *Wdr72* knockout (*Wdr72*$^{-/-}$) mouse model. The mice had a hypomineralized tooth defect, similar to what is observed in humans with *Wdr72*-associated AI. Our immunohistochemical studies of maturation-stage ameloblasts support a role for WDR72 in enamel maturation, possibly related to removal of amelogenin proteins from the matrix to complete mineralization of the tooth enamel.

2. Results

2.1. Identification of a novel 5-base pair deletion in exon 8 of the Wdr72 gene in a family with autosomal recessive Amelogenesis imperfecta (AI)

We identified the 7th reported mutation in *Wdr72* to be associated with an autosomal recessive pattern of inheritance to result in AI (Fig. 1A). Among the affected individuals, the 10.5-year-old proband (V3) illustrated the most severe phenotype, exhibiting yellow-brown staining and hypomature enamel in the permanent dentition (Fig. 1B). His panoramic radiograph revealed unerupted tooth enamel with an apparently normal thickness and an indistinguishable radiopacity to dentin, which is typically less radiopaque than enamel and indicates hypomineralization (Fig. 1C). Primary teeth of the affected identical twin sisters (V4 & V5) at 4-years-old displayed less severe phenotypes, although enamel was largely absent on the occlusal third of all primary teeth (Fig. 1D). Their radiographic images showed erosion of erupted primary molar enamel with similar radiopacities to dentin (Fig. 1E & F). All affected children were highly sensitive to thermal and chemical stimuli. These enamel phenotypes are similar to those described in previous reports of patients with mutated copies of the *Wdr72* gene (Lee et al., 2010; El-Sayed et al., 2011; Wright et al., 2011; Kuechler et al., 2012), all of which predict early stop codons (Fig. 1H).

The proband was also congenitally missing 3 out of 4 six-year-old permanent molars (teeth #3, 19 and 30) and exhibited delayed eruption of his mandibular primary canines and molars, indicating a 1-year delay in dental development (Fig. 1C). Similar tooth development phenotypes have been reported in association with only one other *Wdr72* mutation, the second-most upstream mutation occurring at exon 10 (Fig. 1H) (Kuechler et al., 2012).

We used a candidate gene approach to compare DNA sequences of affected individuals and their immediate family members (Fig. 1A) (Supplementary Table 1). Chromatograms of affected, unaffected, and carrier individuals at exon 8 of the human *Wdr72* gene

(NM_182758. 2) revealed a 5-base pair deletion (c.806_810delGGCAG) that followed an autosomal recessive inheritance pattern of the AI phenotype (Fig. 1G). This exon 8 deletion mutation resulted in a frameshift and premature stop codon (c.806_810delGGCAG; p.G255VfsX294). In addition, single nucleotide polymorphisms (SNPs) were also found to segregate with the deletion mutation, occurring in exon 14 as a silent mutation (c.1865G > A, p.613 V > V; rs74018741) and in the intron between exons 12 and 13 (g.53994305A > G; rs74018741) (Supplementary Table 2). All other variations in sequenced candidate genes (*Amtn*, *Ambn*, *Enam*, *Mmp20*, and *Klk4*) of this family did not follow the disease inheritance (Supplementary Tables 1 & 2).

2.2. WDR72 structure modeling predicted a configuration unique to proteins found in membrane-deformation complexes with homology to the crystallized β′-COP structure

The human full-length WDR72 protein is 1102 amino acids in length and predicts two clusters of WD40 repeat domains at the N-terminus and a unique C-terminus with no identifiable homology domains (Fig. 2A; ENSG00000166415). To provide further insight into WDR72 function, we generated all-atom models of the human full-length WDR72 protein (Fig. 2A) and mutated variants (Supplementary Fig. 1). These models were generated using sequence similarity to annotated proteins using two comparative protein structure prediction pipelines: (1) I-TASSER (Zhang, 2007; Roy et al., 2010) and (2) HHsearch ported into MODELLER (Soding et al., 2005; Zhang, 2007). Among all known protein structures in the Protein Data Bank (PDB), both modeling pipelines showed full-length WDR72 with greatest structural homology to the known crystal structure of *Saccharomyces cerevisiae* β′-COP (Fig. 2B), an essential subunit in eukaryotic COPI vesicle coat assemblies (PDB identifier: 3mkq) and was thus used as the primary template for constructing the WDR72 models. All statistically reliable models of full-length WDR72 (zDOPE < – 1) showed a series of β-sheets folded into two β-propellers, followed by a succession of parallel α-helices twisting into a compact tail, referred to as an α-solenoid (Fig. 2C). This structural iteration of 1 or 2 β-propellers followed by an α-solenoid is unique to membrane-deformation complexes (Lee and Goldberg, 2010; Field et al., 2011), which include vesicle coatomers (i.e. Clathrin, COPII, COPI) and the nuclear pore complex (i.e. Nup).

To evaluate the number of blades present in each β-propeller, we applied the hidden Markov random field algorithm SMURF (Menke et al., 2010), built specifically to detect combinations of 6-, 7-, and 8-bladed double β-propellers. We found that full-length WDR72 was most likely composed of two 7-bladed β-propellers ($P < 0.0001$) rather than any other combinations of one or two 6-, 7- or 8-bladed β-propellers ($P > 0.05$), which is consistent with other membrane-deformation complex proteins. The 1st β-propeller blades were predicted as the following residues: 22–59, 67–104, 119–150, 168–198, 215–251, 260–292, and 301–353; and for the 2nd β-propeller: 359–400, 407–442, 466–494, 521–554, 562–627, 633–659, and 665–686; with α-helices thereafter (Fig. 2C).

We observed that both exon 8 and exon 10 mutations occurred between two predicted WD40-repeat domain clusters (Fig. 2A; ENSG00000166415). Multiple splice variants have been identified for the human *Wdr72* gene, whose encoding is regulated by several different

5′UTRs and 3′UTRs (AceView) (Thierry-Mieg and Thierry-Mieg, 2006). This may suggest evasion of RNA decay in *Wdr72* mutations observed in individuals with AI. Under this possibility, we modeled all putative WDR72 truncations resulting from AI-related mutations and found that these two most up-stream mutations formed a single β-propeller containing only 6 blades ($P < 0.01$), rather than 7, which suggests instability of the protein fold (Supplementary Fig. 1).

2.3. Successful knockout of Wdr72 in mice resulted in hypomaturation enamel phenotypes similar to AI patients with Wdr72 mutations

To further examine the role of *Wdr72* in enamel formation, we established a functional knockout mouse model. The *Wdr72* knockout mouse strain ($Wdr72^{-/-}$) and wild-type littermate controls ($Wdr72^{+/+}$) used in this study were created by breeding heterozygous mice ($Wdr72^{+/-}$) obtained from the Knockout Mouse Project (KOMP) Repository and the Mouse Biology Program at the University of California, Davis. The *Wdr72* mutant allele ($Wdr72^{-}$) was generated using a `knockout first conditional ready' approach using previously published methods (Skarnes et al., 2011), which splices in a *LacZ* gene reporter cassette prior to the critical *Wdr72* exon 3 to all identified *Wdr72* transcripts and thus a functional knockout of *Wdr72* (Fig. 3A).

Mandibular molars and incisors of 6-week-old male $Wdr72^{+/+}$ and $Wdr72^{-/-}$ mice were evaluated for gross morphological differences (Fig. 3C) and exhibited an enamel phenotype similar to that observed in our affected AI patients (Fig. 1B & D). $Wdr72^{-/-}$ mice showed opaque and darkly stained enamel relative to the translucency observed in $Wdr72^{+/+}$ mice (Fig. 3C). $Wdr72^{-/-}$ enamel was of normal thickness at the base of incisors and molar crowns but was lost at occlusal surfaces, while the exposed dentin remained relatively intact. Heterozygous mice ($Wdr72^{+/-}$) appeared to have normal enamel akin to $Wdr72^{+/+}$ mice (data not shown), which mimics the autosomal recessive inheritance pattern seen in AI.

No other obvious tooth phenotypes or differences in major organs known to express *Wdr72* (ie. kidney and brain) were observed in $Wdr72^{-/-}$ mice (data not shown). Whole body weights of $Wdr72^{-/-}$ mice were significantly reduced ($P < 0.05$), beginning at postnatal day 21 (P21) in males and P24 in females compared to their $Wdr72^{+/+}$ controls (Supplementary Fig. 2). Tooth eruption in mice occurs between ages P10 and P14, while weaning age is P21, indicating that these body weight differences were due to difficulties with chewing hard foods rather than systemic effects caused by a loss of *Wdr72*.

Quantitative real-time PCR (qPCR) of micro-dissected secretory and maturation-stage ameloblasts showed significantly reduced *Wdr72* mRNA expression in $Wdr72^{-/-}$ secretory and maturation-stage ameloblasts to 4.4% and 1.8%, respectively, of $Wdr72^{+/+}$ controls ($P < 0.05$). Such relatively low levels of *Wdr72* transcript observed in our mouse model is consistent with leaky expression levels observed for gene trapping methodologies and indicate successful *Wdr72* knockout (Fig. 3D) (Galy et al., 2004). In addition, relative amounts of *Wdr72* transcript were significantly up-regulated from secretory to maturation stage in $Wdr72^{+/+}$ ameloblasts ($P < 0.05$), suggesting a major function during enamel maturation (Fig. 3D).

Similar to our qPCR findings, immunostaining with an antibody made to the CETGTLERHETGERA peptide sequence of the WDR72 protein (amino acids 587–600 plus an extra cysteine residue) illustrated little to no WDR72 present in *Wdr72*$^{-/-}$ ameloblasts (Fig. 4B, D, & F). Verification of our WDR72 antibody, which was made against the same peptide sequence as the one previously synthesized (El-Sayed et al., 2009), was performed on *Wdr72*$^{+/+}$ and *Wdr72*$^{-/-}$ kidneys by western blot (Supplementary Fig. 3). In *Wdr72*$^{+/+}$ mice, ameloblasts showed increased WDR72 immunoreactivity from secretory to maturation stage (Fig. 4A, C, & E). Using the continuously growing mouse incisor to visualize WDR72 expression on a time-scaled spectrum of ameloblast differentiation stages required for enamel formation, we further observed a specific increase at the onset of maturation stage and subcellular localization to distinct vesicle-like puncta at apical and basal regions of the cell (Fig. 4C & E), whereas, immunoreactivity in secretory ameloblasts appeared light and diffuse (Fig. 4A).

2.4. Wdr72$^{-/-}$ mice had enamel phenotypes occurring specifically during the maturation stage, showing a hypomineralized enamel matrix and shortened heights in ameloblasts

Murine mandibles from 6-week-old male *Wdr72*$^{+/+}$ (n = 3) and *Wdr72*$^{-/-}$ mice (n = 3) were scanned by micro-computed tomography (microCT) and analyzed for differences in relative intensities of the major mineralized tissue types (enamel, dentin, and alveolar bone). The process of normal enamel mineralization was observed in the continuously growing mouse incisor of *Wdr72*$^{+/+}$ mice, which showed an increasing enamel radiopacity that coincided with the transition zone of differentiating ameloblasts from secretory to maturation-stage morphologies (Fig. 5A, arrow). In contrast, radiopacity of enamel, beginning at the maturation stage of *Wdr72*$^{-/-}$ molars and incisors, was significantly reduced compared to that of the *Wdr72*$^{+/+}$mice (Fig. 5A & B). These observations were quantified in cross-sections of the mandibular incisor, taken at secretory and maturation stages, and averaged for gray scale values within a selected region of interest (Fig. 5C–F). We found enamel radiopacities of *Wdr72*$^{+/+}$ and *Wdr72*$^{-/-}$ mice were not significantly different at secretory stage ($P = 0.92$) but were significantly reduced at maturation stage in *Wdr72*$^{-/-}$ mice ($P < 0.05$) (Fig. 5E). Interestingly, *Wdr72*$^{-/-}$ enamel from secretory to maturation stages showed significant differences ($P < 0.05$), suggesting that partial mineralization of the enamel matrix still occurred in the absence of *Wdr72*. *Wdr72*$^{-/-}$ dentin ($P = 0.26$) and alveolar bone ($P = 0.22$) did not significantly differ in gray scale values compared to *Wdr72*$^{+/+}$ controls (Fig. 5E).

Hematoxylin and eosin (H&E) stains of *Wdr72*$^{+/+}$ and *Wdr72*$^{-/-}$ male mandibles at P10 showed morphologically normal secretory ameloblasts in *Wdr72*$^{-/-}$ mice and shortened maturation-stage ameloblasts, (Fig. 6). In addition, *Wdr72*$^{-/-}$ mice exhibited retained non-mineralized, organic material in the enamel matrix during maturation stage (Fig. 6, yellow arrows), whereas the lack of this proteinaceous staining in *Wdr72*$^{+/+}$ enamel matrices indicated a more mineralized enamel matrix (Fig. 6A & B).

2.5. Loss of Wdr72 resulted in decreased intracellular amelogenin proteins with no effect on transcript levels

We next investigated the possibility that *Wdr72* was needed for reuptake of amelogenin proteins from the matrix, since our *Wdr72*$^{-/-}$ mice showed retained proteinaceous material in the enamel matrix, and amelogenin is the predominant extracellular matrix protein secreted and hydrolyzed into fragments during enamel formation. Amelogenin immunoreactivity was slightly reduced in secretory stage ameloblasts at the Tomes' processes in *Wdr72*$^{-/-}$ mice (Fig. 7B) and was more obviously reduced at the apical border and the cytoplasm in *Wdr72*$^{-/-}$ ameloblasts at early maturation stage (Fig. 7D) as compared to ameloblasts from *Wdr72*$^{+/+}$ mice (Fig. 7A and C, respectively). By mid-maturation, intracellular amelogenin staining was absent in both *Wdr72*$^{+/+}$ and *Wdr72*$^{-/-}$ ameloblasts (Fig. 7E & F).

To verify that the decreased intracellular amelogenins in *Wdr72*$^{-/-}$ mice was not due to a decrease in amelogenin mRNA production, we quantified amelogenin transcripts from microdissected enamel epithelia at secretory and maturation stages. Analyses by qPCR showed no significant differences between *Wdr72*$^{+/+}$ and *Wdr72*$^{-/-}$ ameloblasts at either stage (n = 3; $P = 0.81$ secretory, $P = 0.53$ maturation) (Fig. 7G).

2.6. Wdr72$^{-/-}$ mice showed reduced immunostaining of the endosome protein CLC5 during the maturation stage compared to other vesicle markers

Consecutive sections of *Wdr72*$^{+/+}$ maturation-stage ameloblasts showed WDR72 and CLC5 immunolocalization to the same supernuclear (basal) areas, as well as to apical regions slightly distal to the enamel matrix border (arrowheads, Fig. 8G & H). In addition, CLC5 was less immunoreactive in *Wdr72*$^{-/-}$ maturation-stage ameloblasts, as compared to *Wdr72*$^{+/+}$ mice (Fig. 8B, D, & F). Unlike CLC5, immunostaining for RAB4A (a marker for endosome sorting and recycling) and LAMP1 (a marker for lysosomes) did not show obvious differences between *Wdr72*$^{+/+}$ and *Wdr72*$^{-/-}$ maturation-stage ameloblasts (Fig. 8I–L).

3. Discussion

The human *Wdr72* gene has a total of 20 exons that contribute to several different transcript variants (ENST00000360509) (Thierry-Mieg and Thierry-Mieg, 2006), the longest and most common of which encodes a protein 1,102 amino acids in length (CCDS 10151.1). *Wdr72* was first found to be a candidate for autosomal recessive amelogenesis imperfecta (AI) in individuals affected with a pigmented and hypomaturation enamel phenotype (AI2A3; MIM 613211) through the use of a single nucleotide polymorphism (SNP) microarray (El-Sayed et al., 2009). Since this discovery, a total of seven *Wdr72* mutations have been reported as causal links to AI, including the 5-base pair deletion that we identified in exon 8 (c. 806_810delGGCAG). Previously reported mutations located farther downstream, spanning exons 10 through 17, are also predicted to disrupt the unique C-terminal domain (exons 15 to 20) by introducing premature stop codons that lead to truncated proteins (El-Sayed et al., 2009; Lee et al., 2010; El-Sayed et al., 2011; Wright et al., 2011; Kuechler et al., 2012). While it is unclear whether any of these mutated *Wdr72* variants are indeed translated as

defective proteins or degraded by nonsense-mediated decay, all mutations lead to similar hypomaturation enamel phenotypes.

In addition to a tooth enamel defect, we observed congenitally missing permanent molars and a one-year delay in tooth development in an individual with our identified exon 8 mutation (Fig. 1C). Similar phenotypes have been reported in only one other *Wdr72* mutation (exon 10) (Kuechler et al., 2012), the second-most upstream to be found in AI (Fig. 1H), possibly linking early *Wdr72* mutations to additional tooth-related defects.

To evaluate the potential functions of WDR72, we used bioinformatics to model a predicted protein structure of WDR72 by mapping the full-length human amino acid sequence onto all known structures within the Protein Data Bank (PDB). Our WDR72 structure model predicted a membrane-coating architecture composed of two 7-bladed β-propeller heads, followed by an α-solenoid fold, which are respectively encoded by two N-terminal WD40-repeat domain clusters and a unique C-terminus (residues #687–1102). This particular domain combination (1 or 2 β-propellers, then α-solenoid) is a highly conserved architecture among proteins that form membrane coat complexes, dating back to the early eukaryotic endomembrane system (Devos et al., 2004; Field et al., 2011). In addition, this group of membrane-coating complexed proteins has remained somewhat exclusive to (a) the scaffold-layer proteins of the nuclear pore complex (Nups) that stabilize the inner and outer nuclear envelope membranes at the nuclear pore edges and (b) the vesicle coatomers (COPI, COPII, and Clathrin) that assemble in cage-like lattices to initiate the budding step of vesicle formation (Devos et al., 2006). Structure domains of these membrane-coating proteins typically utilize their WD40 β-propeller folds to serve as docking sites for multiple protein–protein interactions (Stirnimann et al., 2010; Good et al., 2011; Xu and Min, 2011) and their α-solenoids, formed from anti-parallel stacked α-helices, to stabilize and induce membrane curvature (Devos et al., 2006; Field et al., 2011). Modeling WDR72 as a structure containing these domains, specifically in the β–β–α order, suggests it as a member of this membrane-coating group.

We found that when WDR72 was compared to all solved protein structures, the highest *structural* homology was to β′-COP (PDB identifier: 3mkq), an essential subunit in the COPI vesicle coatomer complex. This homology further suggests that WDR72 functions as a vesicle coat protein, and together these bioinformatic analyses are consistent with the previously proposed role for WDR72 in vesicle trafficking (El-Sayed et al., 2009; Lee et al., 2010). This previously proposed function for WDR72 was based on the high *sequence* homology to WDR7, a known regulator of Rab3A GTPase in Ca^{2+}-dependent exocytosis at neural synapses (Nagano et al., 2002; Kawabe et al., 2003). Interestingly, WDR7 (under the alias “Rabconnectin-3β”) has another function in regulating vesicles, rather, in the endocytic pathway by directly monitoring vacuolar H^{+}-ATPase (v-ATPase) activity in *Drosophila* (Yan et al., 2009; Sethi et al., 2010), indicating that WDR72 may too function in both exocytosis and endocytosis. Further evidence pointing to an endocytic vesicle coat function for WDR72 are the *in vivo* immunolocalization of AP2 (cargo-specifying adaptor component of Clathrin coatomers) found by Lacruz and co-workers (Lacruz et al., 2013). Together, these findings support a role for WDR72 in mediating vesicle formation,

potentially as an endocytic and/or exocytic coat protein to help regulate transport between cell and matrix.

It is also worth noting that WDR72 and WDR7 diverge at residue #845 (exon 15) (Lee et al., 2010), and the remaining 60% of WDR72's C-terminus is unique. The C-terminus is predicted to form the α-solenoid region, and α-solenoids of canonical vesicle coatomers are structurally conserved but exhibit little similarity to one another at the sequence level (Field et al., 2011). These differences are thought to contribute to the diversity of lattice size and shape, which invariably dictate cargo specificities and vesicle type, suggesting that the unique C-terminal sequence of WDR72 specifies its function to enamel formation and its vesicle cargo. The importance of this α-solenoid is emphasized by our modeling of all putative WDR72 proteins containing mutations relevant to hypomaturation enamel AI phenotypes, all of which showed a shortened or absent α-solenoid tail (Supplementary Fig. 1).

To further define the function of WDR72, we generated a knockout mouse (*Wdr72*$^{-/-}$), which exhibited a hypomaturation enamel phenotype similar to that observed in humans with *Wdr72*-associated AI (El-Sayed et al., 2009; Wright et al., 2011; Kuechler et al., 2012). Quantitative RT-PCR (qPCR) of *Wdr72*$^{-/-}$ secretory and maturation-stage ameloblasts showed low mRNA *Wdr72* transcript levels in both tissue groups relative to the observed up-regulation from secretory to maturation stage in *Wdr72*$^{+/+}$ control mice. Similarly, anti-WDR72 immunostaining of *Wdr72*$^{-/-}$ ameloblasts exhibited non-specific background staining at all stages of enamel formation, whereas *Wdr72*$^{+/+}$ controls were intensely immunoreactive shortly after entering the maturation stage. Western blots of *Wdr72*$^{+/+}$ and *Wdr72*$^{-/-}$ kidney samples paralleled these findings with low WDR72 protein levels in *Wdr72*$^{-/-}$ mice.

Whole body weights of both female and male *Wdr72*$^{-/-}$ mice were also decreased compared to *Wdr72*$^{+/+}$ mice, however, this was observed only after weaning age (P21), suggesting that this difference was due to the tooth-related defect as opposed to other systemic effects. Overall, the *Wdr72*$^{-/-}$ mice paralleled the descriptions of individuals with *Wdr72*-related AI. Taken together, these initial characterization studies illustrate that *Wdr72* is functionally knocked out in our *Wdr72*$^{-/-}$ mouse model, providing an excellent system for studying *Wdr72*-associated AI to elucidate its role in tooth development.

Similar to the radiolucent enamel phenotypes described for human *Wdr72* mutations, our microCT imaging of *Wdr72*$^{-/-}$ mandibles showed stage-specific and tissue-specific hypomineralized defects in the tooth enamel. At secretory stage, relative intensities of *Wdr72*$^{-/-}$ enamel radiopacities were comparable to those of *Wdr72*$^{+/+}$ controls but did not increase in radiopacity to the same extent as Wdr72$^{+/+}$ enamel once the maturation stage began. *Wdr72* loss also appeared to have tissue-specific effects, showing dentin and alveolar bone to be unchanged in *Wdr72*$^{-/-}$ mice.

Additional evidence in support of the stage-specificity of WDR72 during enamel maturation were our findings that *Wdr72*$^{-/-}$ ameloblasts appeared shorter in height only after differentiating into the maturation-stage cell type, and the *Wdr72*$^{-/-}$ enamel matrix differed

only during the maturation stage, showing retained organic matter. These comparisons were made along the continuously growing mouse incisor, which presents the entire spectrum of enamel formation (Leblond and Warshawsky, 1979), thus providing time-scale insight into WDR72 function. The observed cell and matrix phenotypes further support a stage-specific role for WDR72 in regulating enamel mineralization and suggests a function in one of the major cell processes in maturation-stage ameloblasts.

A major function of maturation-stage ameloblasts that is often disrupted in AI hypomaturation phenotypes is the processing of amelogenin proteins, which constitute the majority of the organic extracellular matrix (Hart et al., 2004; Kim et al., 2005; Barron et al., 2010). Our observation that organic material was retained in *Wdr72*$^{-/-}$ enamel matrices during maturation suggests that WDR72 has a role in either the secretion of proteases into the mineralizing matrix or in removal of hydrolyzed protein fragments from the matrix to allow final matrix mineralization to occur. Amelogenins are secreted during early matrix formation and are subsequently hydrolyzed and removed from the enamel matrix during the maturation stage to allow thickening of the hydroxyapatite crystals that comprise the tooth enamel (Smith, 1979; Hu et al., 2007; Gibson, 2011). Removal of hydrolyzed matrix proteins, including amelogenins, may be due to either a passive diffusion between the open junctions of smooth-ended ameloblasts or an active transport mechanism through the cells (Nanci et al., 1998). As amelogenins are removed, calcium is transported through ameloblasts and deposited along with phosphate to form the mineralized enamel matrix (Hubbard, 2000).

We found that *Wdr72*$^{-/-}$ maturation-stage ameloblasts had less intracellular amelogenin protein with no change in its relative synthesis compared to *Wdr72*$^{+/+}$ controls, suggesting that WDR72 influences the active uptake of amelogenin fragments into the cell, presumably by regulating endocytosis. Interestingly, we also observed decreased amelogenin immunoreactivity at the Tomes' processes in *Wdr72*$^{-/-}$ secretory ameloblasts with no effect on transcript levels. This was surprising, given that *Wdr72* loss had so far manifested as a maturation stage phenotype; however, it is still consistent with the fact that *Wdr72*$^{+/+}$ secretory ameloblasts express WDR72, albeit at low levels (El-Sayed et al., 2009). Tomes' processes, though largely functioning in the exocytosis of amelogenins, also have endosomes that contain hydrolyzed amelogenins (Smith, 1979; Sasaki, 1984; Nanci et al., 1996). It is also possible that WDR72 has more subtle roles at earlier stages of tooth development that involve intracellular amelogenin transport, which is supported by the tooth agenesis and delayed eruption observed in some AI individuals.

To further investigate the possible vesicle trafficking function of WDR72, we immunostained *Wdr72*$^{+/+}$ and *Wdr72*$^{-/-}$ maturation-stage ameloblasts with anti-CLC5 as a marker of early endosomes, anti-RAB4A as a marker of early and recycling endosomes, and anti-LAMP1 as a marker of lysosomes. Our immunostains of WDR72 and CLC5 on consecutive sections of *Wdr72*$^{+/+}$ maturation-stage ameloblasts suggest that WDR72 localizes to endosomes, which is supported by similar immunolocalizations observed for RAB4A and the endocytic coat protein, AP2 (Lacruz et al., 2013), but not the more basal immunolocalization of LAMP1 to lysosomes.

In *Wdr72*$^{-/-}$ maturation-stage ameloblasts, CLC5 showed decreased immunoreactivity relative to *Wdr72*$^{+/+}$ controls, while RAB4A and LAMP1 appeared to be unaffected. CLC5 and RAB4A are both early endosome markers and are frequently associated with one another (Devuyst et al., 1999), although RAB4A also specifically functions in recycling endosomes. This suggests a unique function for WDR72 in mediating a specific subpopulation of endosomes, possibly related to other known functions of CLC5, such as exocytosis of ion channel antiporters (Lin et al., 2011), Ca^{2+} transport (Luyckx et al., 1998), or pH regulation (Hara-Chikuma et al., 2005; El-Sayed et al., 2011; Duan, 2014) that are integral to major processes carried out by maturation-stage ameloblasts. While it is also possible that CLC5 decreases observed in *Wdr72*$^{-/-}$ ameloblasts were attributed to secondary effects on the cell, these decreases coincided with the timing of normal WDR72 expression.

LAMP1 has been suggested to mediate amelogenin uptake into ameloblasts, and extracellular increases in amelogenin *in vitro* has been shown to upregulate LAMP1 (Le et al., 2007; Shapiro et al., 2007). Therefore, we would expect that if amelogenin uptake into the cell was decreased, LAMP1 immunostaining would also be relatively decreased in *Wdr72*$^{-/-}$ mice. The lack of any change in LAMP1 may suggest that WDR72 does not mediate amelogenin uptake into the cell, but rather is involved in degradation of amelogenins in the extra-cellular matrix, possibly through the secretion of enamel matrix proteinases. Reduced proteinase secretion at the maturation stage could inhibit the uptake of amelogenin protein fragments into the cell. Further analysis of matrix proteinases in Wdr72$^{-/-}$ as compared to Wdr72$^{+/+}$ will further clarify the possible roles of WDR72 in amelogenin degradation and endocytosis.

In summary, these studies have reported the use of structural modeling to support a function of WDR72 in vesicle trafficking. The generation and initial analyses of the *Wdr72*$^{-/-}$ mouse confirmed the importance of WDR72 in enamel formation and illustrated a direct link between mutated WDR72 to hypomineralized enamel. We found reduced intracellular amelogenin in the *Wdr72*$^{-/-}$ ameloblasts with a similar reduction in the endosome marker protein ClC5, suggesting a role for WDR72 in the removal of amelogenins during enamel maturation. Further understanding of WDR72's function in amelogenesis will allow us to better understand this unique biomineralization process and how other tissues potentially regulate mineralization. These studies are also important in determining other yet unknown risk factors for AI patients affected with mutated *Wdr72*.

4. Methods

4.1. Mutation screening

A consanguineous family exhibiting hypomature phenotypes of autosomal recessive inheritance Amelogenesis Imperfecta (AI) was examined at the UCSF pediatric dental clinic and screened for mutations using a candidate gene approach. DNA samples of the probands and all immediate family members were obtained using Oragene®DNA sample collection kit (DNA Genotek, Inc., Ontario, Canada) with approval by the UCSF Committee on Human Research. Forward and reverse primers were designed within introns to flank coding regions and potential splice sites in ameloblastin (*Ambn*), amelogenin (*AmelX*), amelotin

(*Amtn*), enamelin (*Enam*), kallekrein-related peptidase 4 (*Klk4*), matrix metalloproteinase-20 (*Mmp20*), and WD repeat-containing protein 72 (*Wdr72*) (Supplementary Table 1). Polymerase chain-reaction (PCR) amplifications of these candidate genes were performed using taq polymerase (Invitrogen, Carlsbad, CA), and sequencing was conducted at Elim Biopharmaceuticals (Hayward, CA). DNA sequence assemblies and SNP analyses (Supplementary Table 2) were performed and documented with CodonCode Aligner software (Centerville, MA).

4.2. Protein structure modeling

The WDR72 sequence was downloaded with accession identifier Q3MJ13 from the UniProt knowledgebase (Apweiler et al., 2004). To generate atomic models for WDR72 wild type and mutant structures, we applied the iterative threading assembler (I-TASSER) (Zhang, 2007) and the restraint-based comparative modeling program MODELLER-v9.10 (Sali and Blundell, 1993) with alignments generated by the profile alignment homology alignment algorithm HHpred (Soding et al., 2005). Models were generated with the automated modeling pipelines accessible through the I-TASSER webserver (http://zhanglab.ccmb.med.umich.edu/I-TASSER/) (Zhang, 2007; Roy et al., 2010) and the bioinformatics toolkit (http://toolkit.tuebingen. mpg.de/hhpred) (Soding et al., 2005), respectively. These two pipelines model diverse crystallized proteins with an average structural alignment GDT-TS measure (range 0–100) (Zemla et al., 2001) of 70 in blinded assessments, outperforming all other automated protein structure prediction tools (Mariani et al., 2011). To verify double seven-bladed β propeller fold topology for WDR72, we applied the β-propeller blade structural motif algorithm SMURF (Menke et al., 2010).

WDR72 oligomer models were generated with the multi-scale modeling and structural comparison tools in Chimera (Yang et al., 2012) by comparison of monomer models to crystallographic structures of structurally homologous protein oligomers found by HHpred.

4.3. Knockout mouse generation

The *Wdr72* knockout mouse strain used in this study was created from an ES cell clone (EPD0085_5_D06) generated by the Welcome Trust Sanger Institute and injected into a pregnant female mouse blastocyst by the KOMP Repository and the Mouse Biology Program at the University of California, Davis. The *Wdr72* mutant allele (*Wdr72*$^{-}$) was created using a `knockout first conditional ready' approach using previously published methods (Skarnes et al., 2011), generating a functional knockout through splicing in *LacZ* gene reporter and Neomycin (*Neo*) selection cassettes (Fig. 3A). The targeting vector incorporated an En2 splice acceptor (SA) and internal ribosome entry site (IRES) upstream of *LacZ*, followed by a polyadenylation (pA) signal. A *loxP* site separated the *LacZ* cassette from the subsequent *Neo* resistance cassette, which was driven by an autonomous promoter (hBactP) and pA signal. Flippase recognition target (*FRT*) sites flanked both *LacZ* and *Neo* cassettes, all of which was inserted between exons 2 and 3. Two additional *loxP* sites were introduced on either side of exon 3.

Heterozygous mice (*Wdr72*$^{+/-}$) on a C57BL/6 genetic background were purchased and subsequently bred to generate the knockout (*Wdr72*$^{-/-}$) and wild-type (*Wdr72*$^{+/+}$) mice used

in these experiments. Genotypes of mice were determined by standard and quantitative PCR (Transnetyx, Cordova, TN) using genomic DNA obtained from tail biopsies with forward primers: *NeoF*-GGGATCTCATGCTGGAGTTCTTCG, *F*-TCTTTCACCTAAGCAACACATGCGG, and reverse primer *R*-GAAACCCGGAGATGAAGGAATGTGC. Amplicon sizes of $Wdr72^{+}$ and $Wdr72^{-}$ alleles were 520 and 633 bp, respectively.

4.4. RNA isolation and quantitative real-time PCR

Total RNA was isolated from dissected flash-frozen kidneys and from micro-dissected secretory and maturation-stage ameloblasts of $Wdr72^{+/+}$ and $Wdr72^{-/-}$ mice at postnatal day 24 using RNeasy Mini kit (QIAGEN, Germantown, MD). Aliquot containing 20 μg of total RNA was reverse transcribed to cDNA using SuperScript® III Reverse Transcriptase and oligo dT primers (Invitrogen, Carlsbad, CA). For kidney samples, polymerase chain reaction amplification for standard PCR was performed with the Hot Start Taq kit (Qiagen) by first incubating the reaction mixture at 95° for 5 min, followed by 94 °C, 57 °C, and 72 °C for 1 min each for 35 cycles and then 72 °C for 10 min. The primers used flanked the exon–exon boundaries surrounding exon 14 of the *Wdr72* transcript (ENST00000360509), targeting the epitope region to where our WDR72 antibody would recognize. Primers were designed using Frodo (http://frodo.wi.mit.edu/primer3/) (Koressaar and Remm, 2007; Untergasser et al., 2012). The products were visualized on a 1.7% agarose gel with SYBR GREEN staining (Invitrogen, Carlsbad, CA). Real-time PCR gene expression was characterized by quantitative PCR using the ABI 7500 system (Applied Biosystems, Carlsbad, CA). cDNA was amplified with the Fast Start SYBR Green master mix (Roche, Indianapolis, IN). Relative expression levels of target genes were analyzed by the delta-Ct method as published previously (Thomsen et al., 2010) using GAPDH or 18S as endogenous controls.

4.5. Micro-computed tomography (microCT)

Mineral density levels of 6-week-old undecalcified $Wdr72^{+/+}$ (n = 3) and $Wdr72^{-/-}$ (n = 3) murine hemimandibles were scanned and compared by microCT (SkyScan1076; Bruker-microCT, Kontich, Belgium). X-ray source operating settings were set to 50 kV and 160 μA and image reconstitution was carried out with NRecon software (Bruker-microCT). Using Amira software (ver 1.4.1 SkyScan), coronal sections perpendicular to the curve of the incisor and in line with the midsagittal plane of the incisor were selected from 3D reconstructions for quantitative densitometry (g/cm^2) analyses. We compared $Wdr72^{+/+}$ and $Wdr72^{-/-}$ coronal sections landmarked at either the mesial root of the first molar (maturation stage) or the distal root of the third molar (secretory stage) with indexed and normalized gray scale levels (range 0–255). A region of interest (ie. enamel, dentin or alveolar bone) was selected from each coronal section and quantified for mineral density by measuring the average of relative gray values at each pixel within the selected region (ImageJ, ver 1.46r). These gray value outputs were then averaged across samples and compared by paired Students' *t*-tests with a statistical significance threshold of $P < 0.05$.

4.6. Histology

Dissected *Wdr72*$^{+/+}$ and *Wdr72*$^{-/-}$ mandibles at P10 were immediately immerse-fixed in 4% paraformaldehyde (PFA)/0.06 M cacodylate buffer (pH 7.3) overnight and decalcified in 8% EDTA (pH 7.2) for two weeks at 4 °C. Samples were then dehydrated and paraffin-processed for routine embedding and sectioning. Sagittal incisor sections at 5 μm were utilized for standard hematoxylin and eosin (H&E) staining or for immunohistochemistry.

Immunostained tissue sections were deparaffinized and rehydrated, followed by incubation with 10% swine serum for blocking. Primary antibodies targeting WDR72, amelogenin, or CLC5 were incubated at 25 °C overnight, followed by a biotinylated secondary antibody (Dako, Carpinteria, CA) at 25 °C for 1 hr. Alkaline phosphatase conjugated to streptavidin (Vector Laboratories Inc., Burlingame, CA) was used to visualize the colorimetric reaction. Sections were then counterstained using methyl green (Dako, Carpinteria, CA).

The polyclonal rabbit anti-WDR72 antibody was synthesized by Genscript (Piscataway, NJ) from a synthetic peptide (CETGTLERHETGERA) as previously described (El-Sayed et al., 2009), and was used at a 2.7 μg/mL concentration. The rabbit anti-amelogenin antibody (1:500 dilution) was developed in our laboratory as previously described (Le et al., 2007; Li et al., 1998). Purchased antibodies used in this study included polyclonal rabbit anti-CLC5 (Novus Biologicals, Littleton, CO) (NBP1-70374) at a 1:800 dilution, polyclonal rabbit anti-RAB4A (Santa Cruz Biotechnology, Santa Cruz, CA) (sc-312) at 1 μg/mL concentration. The monoclonal rat anti-LAMP1 antibody (1D4B; 1 μg/mL concentration) developed by J. Thomas August was obtained from the Developmental Studies Hybridoma Bank under the auspices of the NICHD and maintained by the University of Iowa, Department of Biology (Iowa Cita, IA 52242). Negative controls were performed with normal rabbit IgG (Vector Laboratories Inc., Burlingame, CA) (I-1000) at matching concentrations to the experimental diluted primary antibodies. Histological images were taken with a Nikon Eclipse E3800 microscope (Melville, NY) using a digital camera (QImaging Inc., Surrey, Canada) and SimplePCI imaging software version 5.3.1.

Supplementary Material

Refer to Web version on PubMed Central for supplementary material.

Acknowledgments

Thank you to our AI patients and family members for contributing samples for this study. In addition, we would like to acknowledge Dr. Neil Katsura for providing the clinical evaluations of the AI patients' radiographs and Dr. Yuki Mochida for the comparative discussions of rodent *Wdr72* knockout models. MicroCT imaging work was performed by Sabra Djomehri at the Division of Biomaterials and Bioengineering MicroCT Imaging Facility, UCSF, generously supported by the Department of Health and Human Services/NIH S10 Shared Instrumentation Grant (S10RR026645), and Departments of Preventive and Restorative Dental Sciences and Orofacial Sciences, School of Dentistry, UCSF. This research was funded by the UCSF Department of Oral and Craniofacial Sciences, NIDCR 1R03 DE019682 and UCSF Start-up Fund to T.L., and NIDCR T32 DE007306 to P.D.

References

Apweiler R, Bairoch A, Wu CH, Barker WC, Boeckmann B, Ferro S, Gasteiger E, Huang H, Lopez R, Magrane M, Martin MJ, Natale DA, O'Donovan C, Redaschi N, Yeh L-SL. UniProt: the Universal

Protein knowledgebase. Nucleic Acids Res. 2004; 32:D115–D119. http://dx.doi.org/10.1093/nar/gkh131. [PubMed: 14681372]

Barron MJ, Brookes SJ, Kirkham J, Shore RC, Hunt C, Mironov A, Kingswell NJ, Maycock J, Shuttleworth CA, Dixon MJ. A mutation in the mouse Amelx tri-tyrosyl domain results in impaired secretion of amelogenin and phenocopies human X-linked amelogenesis imperfecta. Hum. Mol. Genet. 2010; 19:1230–1247. [PubMed: 20067920]

Devos D, Dokudovskaya S, Alber F, Williams R, Chait BT, Sali A, Rout MP. Components of coated vesicles and nuclear pore complexes share a common molecular architecture. PLoS Biol. 2004; 2:e380. [PubMed: 15523559]

Devos D, Dokudovskaya S, Williams R, Alber F, Eswar N, Chait BT, Rout MP, Sali A. Simple fold composition and modular architecture of the nuclear pore complex. Proc. Natl. Acad. Sci. U. S. A. 2006; 103:2172–2177. [PubMed: 16461911]

Devuyst O, Christie PT, Courtoy PJ, Beauwens R, Thakker RV. Intra-renal and subcellular distribution of the human chloride channel, CLC-5, reveals a pathophysiological basis for Dent's disease. Hum. Mol. Genet. 1999; 8:247–257. [PubMed: 9931332]

Ding Y, Estrella MR, Hu YY, Chan HL, Zhang HD, Kim JW, Simmer JP, Hu JC. Fam83h is associated with intracellular vesicles and ADHCAI. J. Dent. Res. 2009; 88:991–996. [PubMed: 19828885]

Duan X. Ion channels, channelopathies, and tooth formation. J. Dent. Res. 2014; 93:117–125. [PubMed: 24076519]

El-Sayed W, Parry DA, Shore RC, Ahmed M, Jafri H, Rashid Y, Al-Bahlani S, Al Harasi S, Kirkham J, Inglehearn CF, Mighell AJ. Mutations in the beta propeller WDR72 cause autosomal-recessive hypomaturation amelogenesis imperfecta. Am. J. Hum. Genet. 2009; 85:699–705. [PubMed: 19853237]

El-Sayed W, Shore RC, Parry DA, Inglehearn CF, Mighell AJ. Hypomaturation amelogenesis imperfecta due to WDR72 mutations: a novel mutation and ultrastructural analyses of deciduous teeth. Cells Tissues Organs. 2011; 194:60–66. [PubMed: 21196691]

Field MC, Sali A, Rout MP. Evolution: On a bender—BARs, ESCRTs, COPs, and finally getting your coat. J. Cell Biol. 2011; 193:963–972. [PubMed: 21670211]

Franceschini N, Haack K, Almasy L, Laston S, Lee ET, Best LG, Fabsitz RR, MacCluer JW, Howard BV, Umans JG, Cole SA. Generalization of associations of kidney-related genetic loci to American Indians. Clin. J. Am. Soc. Nephrol. 2014; 9:150–158. [PubMed: 24311711]

Galy B, Ferring D, Benesova M, Benes V, Hentze MW. Targeted mutagenesis of the murine IRP1 and IRP2 genes reveals context-dependent RNA processing differences in vivo. RNA. 2004; 10:1019–1025. [PubMed: 15208438]

Gibson CW. The amelogenin proteins and enamel development in humans and mice. J. Oral Biosci. 2011; 53:248–256. [PubMed: 22215951]

Good MC, Zalatan JG, Lim WA. Scaffold proteins: hubs for controlling the flow of cellular information. Science. 2011; 332:680–686. [PubMed: 21551057]

Hara-Chikuma M, Wang Y, Guggino SE, Guggino WB, Verkman AS. Impaired acidification in early endosomes of ClC-5 deficient proximal tubule. Biochem. Biophys. Res. Commun. 2005; 329:941–946. [PubMed: 15752747]

Hart PS, Hart TC, Michalec MD, Ryu OH, Simmons D, Hong S, Wright JT. Mutation in kallikrein 4 causes autosomal recessive hypomaturation amelogenesis imperfecta. J. Med. Genet. 2004; 41:545–549. [PubMed: 15235027]

Hertel JK, Johansson S, Raeder H, Platou CG, Midthjell K, Hveem K, Molven A, Njolstad PR. Evaluation of four novel genetic variants affecting hemoglobin A1c levels in a population-based type 2 diabetes cohort (the HUNT2 study). BMC Med. Genet. 2011; 12:20. [PubMed: 21294870]

Hu JC, Chun YH, Al Hazzazzi T, Simmer JP. Enamel formation and amelogenesis imperfecta. Cells Tissues Organs. 2007; 186:78–85. [PubMed: 17627121]

Hubbard MJ. Calcium transport across the dental enamel epithelium. Crit. Rev. Oral Biol. Med. 2000; 11:437–466. [PubMed: 11132765]

Kantaputra PN, Kaewgahya M, Khemaleelakul U, Dejkhamron P, Sutthimethakorn S, Thongboonkerd V, Iamaroon A. Enamel–renal–gingival syndrome and FAM20A mutations. Am. J. Med. Genet. A. 2014; 164A:1–9. [PubMed: 24259279]

Kawabe H, Sakisaka T, Yasumi M, Shingai T, Izumi G, Nagano F, Deguchi-Tawarada M, Takeuchi M, Nakanishi H, Takai Y. A novel rabconnectin-3-binding protein that directly binds a GDP/GTP exchange protein for Rab3A small G protein implicated in Ca(2+)-dependent exocytosis of neurotransmitter. Genes Cells. 2003; 8:537–546. [PubMed: 12786944]

Kim JW, Simmer JP, Hart TC, Hart PS, Ramaswami MD, Bartlett JD, Hu JC. MMP-20 mutation in autosomal recessive pigmented hypomaturation amelogenesis imperfecta. J. Med. Genet. 2005; 42:271–275. [PubMed: 15744043]

Koressaar T, Remm M. Enhancements and modifications of primer design program Primer3. Bioinformatics. 2007; 23:1289–1291. http://dx.doi.org/10.1093/bioinformatics/btm091. [PubMed: 17379693]

Kottgen A, Pattaro C, Boger CA, Fuchsberger C, Olden M, Glazer NL, Parsa A, Gao X, Yang Q, Smith AV, O'Connell JR, Li M, Schmidt H, Tanaka T, Isaacs A, Ketkar S, Hwang SJ, Johnson AD, Dehghan A, Teumer A, Pare G, Atkinson EJ, Zeller T, Lohman K, Cornelis MC, Probst-Hensch NM, Kronenberg F, Tonjes A, Hayward C, Aspelund T, Eiriksdottir G, Launer LJ, Harris TB, Rampersaud E, Mitchell BD, Arking DE, Boerwinkle E, Struchalin M, Cavalieri M, Singleton A, Giallauria F, Metter J, de Boer IH, Haritunians T, Lumley T, Siscovick D, Psaty BM, Zillikens MC, Oostra BA, Feitosa M, Province M, de Andrade M, Turner ST, Schillert A, Ziegler A, Wild PS, Schnabel RB, Wilde S, Munzel TF, Leak TS, Illig T, Klopp N, Meisinger C, Wichmann HE, Koenig W, Zgaga L, Zemunik T, Kolcic I, Minelli C, Hu FB, Johansson A, Igl W, Zaboli G, Wild SH, Wright AF, Campbell H, Ellinghaus D, Schreiber S, Aulchenko YS, Felix JF, Rivadeneira F, Uitterlinden AG, Hofman A, Imboden M, Nitsch D, Brandstatter A, Kollerits B, Kedenko L, Magi R, Stumvoll M, Kovacs P, Boban M, Campbell S, Endlich K, Volzke H, Kroemer HK, Nauck M, Volker U, Polasek O, Vitart V, Badola S, Parker AN, Ridker PM, Kardia SL, Blankenberg S, Liu Y, Curhan GC, Franke A, Rochat T, Paulweber B, Prokopenko I, Wang W, Gudnason V, Shuldiner AR, Coresh J, Schmidt R, Ferrucci L, Shlipak MG, van Duijn CM, Borecki I, Kramer BK, Rudan I, Gyllensten U, Wilson JF, Witteman JC, Pramstaller PP, Rettig R, Hastie N, Chasman DI, Kao WH, Heid IM, Fox CS. New loci associated with kidney function and chronic kidney disease. Nat. Genet. 2010; 42:376–384. [PubMed: 20383146]

Kuechler A, Hentschel J, Kurth I, Stephan B, Prott EC, Schweiger B, Schuster A, Wieczorek D, Ludecke HJ. A novel homozygous WDR72 mutation in two siblings with amelogenesis imperfecta and mild short stature. Mol. Syndromol. 2012; 3:223–229. [PubMed: 23293580]

Lacruz RS, Brookes SJ, Wen X, Jimenez JM, Vikman S, Hu P, White SN, Lyngstadaas SP, Okamoto CT, Smith CE, Paine ML. Adaptor protein complex 2-mediated, clathrin-dependent endocytosis, and related gene activities, are a prominent feature during maturation stage amelogenesis. J. Bone Miner. Res. 2013; 28:672–687. [PubMed: 23044750]

Le TQ, Zhang Y, Li W, Denbesten PK. The effect of LRAP on enamel organ epithelial cell differentiation. J. Dent. Res. 2007; 86:1095–1099. [PubMed: 17959903]

LeBlanc M, Kulle B, Sundet K, Agartz I, Melle I, Djurovic S, Frigessi A, Andreassen OA. Genome-wide study identifies PTPRO and WDR72 and FOXQ1-SUMO1P1 interaction associated with neurocognitive function. J. Psychiatr. Res. 2012; 46:271–278. [PubMed: 22126837]

Leblond CP, Warshawsky H. Dynamics of enamel formation in the rat incisor tooth. J. Dent. Res. 1979; 58:950–975. [PubMed: 283137]

Lee C, Goldberg J. Structure of coatomer cage proteins and the relationship among COPI, COPII, and clathrin vesicle coats. Cell. 2010; 142:123–132. [PubMed: 20579721]

Lee SK, Seymen F, Lee KE, Kang HY, Yildirim M, Tuna EB, Gencay K, Hwang YH, Nam KH, De La Garza RJ, Hu JC, Simmer JP, Kim JW. Novel WDR72 mutation and cytoplasmic localization. J. Dent. Res. 2010; 89:1378–1382. [PubMed: 20938048]

Li W, Mathews C, Gao C, DenBesten PK. Identification of two additional exons at the 3' end of the amelogenin gene. Arch. Oral Biol. 1998; 43:497–504. [PubMed: 9717587]

Lin Z, Jin S, Duan X, Wang T, Martini S, Hulamm P, Cha B, Hubbard A, Donowitz M, Guggino SE. Chloride channel (Clc)-5 is necessary for exocytic trafficking of Na+/H + exchanger 3 (NHE3). J. Biol. Chem. 2011; 286:22833–22845. [PubMed: 21561868]

Luyckx VA, Goda FO, Mount DB, Nishio T, Hall A, Hebert SC, Hammond TG, Yu AS. Intrarenal and subcellular localization of rat CLC5. Am. J. Physiol. 1998; 275:F761–F769. [PubMed: 9815133]

Mariani V, Kiefer F, Schmidt T, Haas J, Schwede T. Assessment of template based protein structure predictions in CASP9. Proteins. 2011; 79(Suppl 10):37–58. http://dx.doi.org/10.1002/prot.23177. [PubMed: 22002823]

Menke M, Berger B, Cowen L. Markov random fields reveal an N-terminal double beta-propeller motif as part of a bacterial hybrid two-component sensor system. Proc. Natl. Acad. Sci. U. S. A. 2010; 107:4069–4074. [PubMed: 20147619]

Nagano F, Kawabe H, Nakanishi H, Shinohara M, Deguchi-Tawarada M, Takeuchi M, Sasaki T, Takai Y. Rabconnectin-3, a novel protein that binds both GDP/GTP exchange protein and GTPase-activating protein for Rab3 small G protein family. J. Biol. Chem. 2002; 277:9629–9632. [PubMed: 11809763]

Nanci A, Fortin M, Ghitescu L. Endocytotic functions of ameloblasts and odonto-blasts: immunocytochemical and tracer studies on the uptake of plasma proteins. Anat. Rec. 1996; 245:219–234. [PubMed: 8769665]

Nanci A, Zalzal S, Lavoie P, Kunikata M, Chen W, Krebsbach PH, Yamada Y, Hammarstrom L, Simmer JP, Fincham AG, Snead ML, Smith CE. Comparative immunochemical analyses of the developmental expression and distribution of ameloblastin and amelogenin in rat incisors. J. Histochem. Cytochem. 1998; 46:911–934. [PubMed: 9671442]

Parry DA, Brookes SJ, Logan CV, Poulter JA, El-Sayed W, Al-Bahlani S, Al Harasi S, Sayed J, Raif el M, Shore RC, Dashash M, Barron M, Morgan JE, Carr IM, Taylor GR, Johnson CA, Aldred MJ, Dixon MJ, Wright JT, Kirkham J, Inglehearn CF, Mighell AJ. Mutations in C4orf26, encoding a peptide with in vitro hydroxyapatite crystal nucleation and growth activity, cause amelogenesis imperfecta. Am. J. Hum. Genet. 2012; 91:565–571. [PubMed: 22901946]

Parry DA, Poulter JA, Logan CV, Brookes SJ, Jafri H, Ferguson CH, Anwari BM, Rashid Y, Zhao H, Johnson CA, Inglehearn CF, Mighell AJ. Identification of mutations in SLC24A4, encoding a potassium-dependent sodium/calcium exchanger, as a cause of amelogenesis imperfecta. Am. J. Hum. Genet. 2013; 92:307–312. [PubMed: 23375655]

Paterson AD, Waggott D, Boright AP, Hosseini SM, Shen E, Sylvestre MP, Wong I, Bharaj B, Cleary PA, Lachin JM, Below JE, Nicolae D, Cox NJ, Canty AJ, Sun L, Bull SB. A genome-wide association study identifies a novel major locus for glycemic control in type 1 diabetes, as measured by both A1C and glucose. Diabetes. 2010; 59:539–549. [PubMed: 19875614]

Roy A, Kucukural A, Zhang Y. I-TASSER: a unified platform for automated protein structure and function prediction. Nat. Protoc. 2010; 5:725–738. [PubMed: 20360767]

Sali A, Blundell TL. Comparative protein modelling by satisfaction of spatial restraints. J. Mol. Biol. 1993; 234:779–815. http://dx.doi.org/10.1006/jmbi.1993.1626. [PubMed: 8254673]

Sasaki T. Endocytotic pathways at the ruffled borders of rat maturation amelo-blasts. Histochemistry. 1984; 80:263–268. [PubMed: 6427140]

Sethi N, Yan Y, Quek D, Schupbach T, Kang Y. Rabconnectin-3 is a functional regulator of mammalian Notch signaling. J. Biol. Chem. 2010; 285:34757–34764. [PubMed: 20810660]

Shapiro JL, Wen X, Okamoto CT, Wang HJ, Lyngstadaas SP, Goldberg M, Snead ML, Paine ML. Cellular uptake of amelogenin, and its localization to CD63, and Lamp1-positive vesicles. Cell. Mol. Life Sci. 2007; 64:244–256. [PubMed: 17187173]

Skarnes WC, Rosen B, West AP, Koutsourakis M, Bushell W, Iyer V, Mujica AO, Thomas M, Harrow J, Cox T, Jackson D, Severin J, Biggs P, Fu J, Nefedov M, de Jong PJ, Stewart AF, Bradley A. A conditional knockout resource for the genome-wide study of mouse gene function. Nature. 2011; 474:337–342. [PubMed: 21677750]

Smith CE. Ameloblasts: secretory and resorptive functions. J. Dent. Res. 1979; 58:695–707. [PubMed: 283112]

Soding J, Biegert A, Lupas AN. The HHpred interactive server for protein homology detection and structure prediction. Nucleic Acids Res. 2005; 33:W244–W248. [PubMed: 15980461]

Stirnimann CU, Petsalaki E, Russell RB, Muller CW. WD40 proteins propel cellular networks. Trends Biochem. Sci. 2010; 35:565–574. [PubMed: 20451393]

Thierry-Mieg D, Thierry-Mieg J. AceView: a comprehensive cDNA-supported gene and transcripts annotation. Genome Biol. 2006; 7(Suppl. 1, S12):11–14.

Thomsen RR, Sølvsten CAEC, Linnet TET, Blechingberg JJ, Nielsen ALA. Analysis of qPCR data by converting exponentially related Ct values into linearly related X0 values. J. Bioinform. Comput. Biol. 2010; 8:885–900. [PubMed: 20981893]

Untergasser A, Cutcutache I, Koressaar T, Ye J, Faircloth BC, Remm M, Rozen SG. Primer3—new capabilities and interfaces. Nucleic Acids Res. 2012; 40:e115–e115. http://dx.doi.org/10.1093/nar/gks596. [PubMed: 22730293]

Vasan RS, Larson MG, Aragam J, Wang TJ, Mitchell GF, Kathiresan S, Newton-Cheh C, Vita JA, Keyes MJ, O'Donnell CJ, Levy D, Benjamin EJ. Genome-wide association of echocardiographic dimensions, brachial artery endothelial function and treadmill exercise responses in the Framingham Heart Study. BMC Med. Genet. 2007; 8(Suppl. 1):S2. [PubMed: 17903301]

Wang SK, Reid BM, Dugan SL, Roggenbuck JA, Read L, Aref P, Taheri AP, Yeganeh MZ, Simmer JP, Hu JC. FAM20A mutations associated with enamel renal syndrome. J. Dent. Res. 2014; 93:42–48. [PubMed: 24196488]

Wright JT, Torain M, Long K, Seow K, Crawford P, Aldred MJ, Hart PS, Hart TC. Amelogenesis imperfecta: genotype-phenotype studies in 71 families. Cells Tissues Organs. 2011; 194:279–283. [PubMed: 21597265]

Xu C, Min J. Structure and function of WD40 domain proteins. Protein Cell. 2011; 2:202–214. [PubMed: 21468892]

Yan Y, Denef N, Schupbach T. The vacuolar proton pump, V-ATPase, is required for notch signaling and endosomal trafficking in Drosophila. Dev. Cell. 2009; 17:387–402. [PubMed: 19758563]

Yang Z, Lasker K, Schneidman-Duhovny D, Webb B, Huang CC, Pettersen EF, Goddard TD, Meng EC, Sali A, Ferrin TE. UCSF Chimera, MODELLER, and IMP: an integrated modeling system. J. Struct. Biol. 2012; 179:269–278. http://dx.doi.org/10.1016/j.jsb.2011.09.006. [PubMed: 21963794]

Zemla A, Venclovas, Moult J, Fidelis K. Processing and evaluation of predictions in CASP4. Proteins. 2001; (Suppl 5):13–21. [PubMed: 11835478]

Zhang Y. Template-based modeling and free modeling by I-TASSER in CASP7. Proteins. 2007; 69(Suppl. 8):108–117. [PubMed: 17894355]

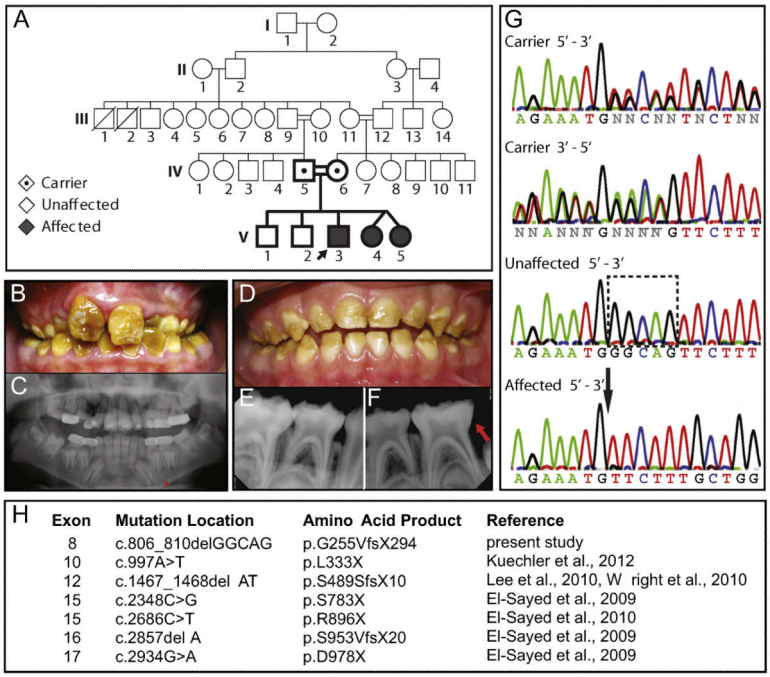

Fig. 1. Identification of a novel 5-base pair deletion in exon 8 of the Wdr72 gene in patients affected with autosomal recessive AI of a pigmented and hypomaturation phenotype

(A) Family pedigree with autosomal recessive inheritance of Amelogenesis imperfecta (AI). Double lines (=) symbolize consanguineous unions, black arrow denotes the proband, emboldened shapes identify family members analyzed for DNA sequencing. (B) Permanent dentition of the male proband (V3; 10.5 y.o.) was pigmented yellowish-brown with a loss of tooth enamel at the surface. (C) The proband's panoramic radiograph revealed hypomineralized enamel in unerupted teeth, missing first permanent molars (teeth #3, 19 and 30), and delayed eruption sequences in primary canines and molars (red asterisk). (D) Representative photograph of one affected twin sister (V4; 4 y.o.) showing primary dentition also exhibiting a hypomaturation enamel phenotype on the occlusal surfaces of erupted teeth. (E, F) Lower PAs also showed a loss of enamel in erupted teeth with similar radiopacity to dentin, indicating hypomineralization (red arrow). (G) Comparisons of representative chromatograms for carrier, unaffected, and affected individuals revealed a 5-base pair deletion in affected patients, which localized to exon 8 of the Wdr72 gene and matched with the AI phenotype. The dotted box encompasses the nucleotides absent in affected patients with a black arrow pointing to the deletion site. (H) List of reported Wdr72 mutations in association with AI.

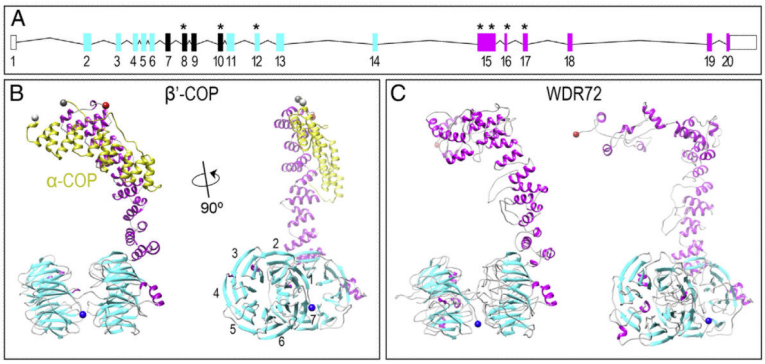

Fig. 2. WDR72 adopts the β-propeller and α-solenoid fold configuration characteristic of membrane-deformation complexes

(A) The human *Wdr72* gene with predicted WD40 domains (cyan boxes) and sequence homology divergence to all other human genes (magenta boxes). Reported mutations associated with Amelogenesis Imperfecta are denoted with an asterisk (*), showing our identified exon 8 mutation in between two clusters of WD40 repeat domains (ENST00000360509). Mutation positions based on CCDC 10151.1; numbered box, *Wdr72* exon; line, intron; empty box, untranslated region (UTR). (B) Monomeric structure of β′-COP protein interacting with the C-terminus of α-COP (yellow), another subunit of the crystallized Saccharomyces cerevisiae COPI triskelion vesicle coat complex (PDB identifier: 3mkq). The side view of β′-COP (right) depicts what is referred to as a βeta-propeller structure (cyan) and an α-solenoid tail (magenta) unique to proteins that interact with curved lipid bilayers. This β′-COP structure was used as a template for model building, as it showed the greatest similarity to WDR72 compared to any other solved protein structures. Numbers represent blades #1–7 that comprise a single β-propeller. (C) Constructed model of WDR72 showing two β-propeller domains and a curved α-solenoid tail. The side view of full-length WDR72 (right) depicts two β-propellers, each with 7 blades (cyan), and a series of α-helices (magenta) forming an α-solenoid tail. Blue sphere, N-terminus; red sphere, C-terminus. (For interpretation of the references to color in this figure legend, the reader is referred to the web version of this article.)

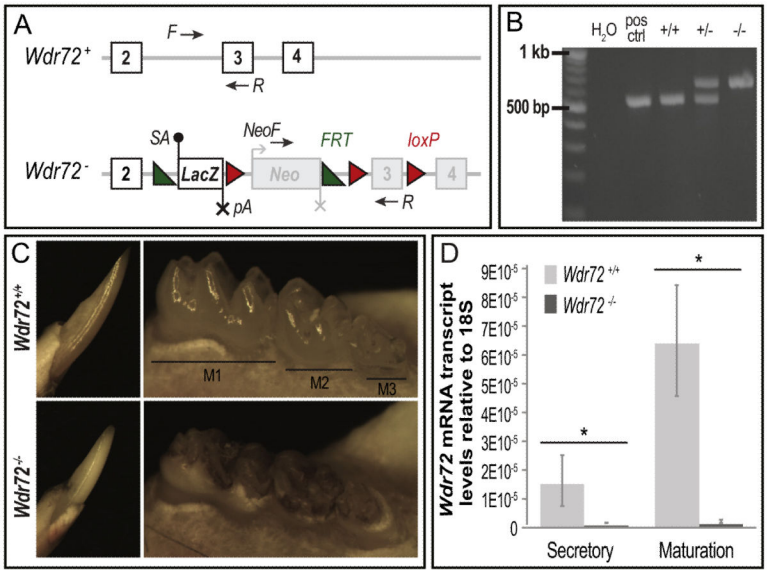

Fig. 3. Successful Wdr72$^{-/-}$ mouse model exhibits hypomaturation enamel phenotypes

(A) *Wdr72* wildtype (+) and mutant (−) allelic variants. The *Wdr72* mutant allele (*Wdr72*$^{-}$) is a functional knockout through splicing in a LacZ gene reporter containing a high affinity splice acceptor (SA, black dot) and termination sequence (pA, black X) prior to the critical exon 3. The encoded mutant transcript is a truncated *Wdr72* at exon 2 fused to *LacZ*. Neomycin (*Neo*) is independently regulated, containing its own promotor (gray bent arrow) and termination sequence (gray X). Numbered white boxes represent coded exons under the *Wdr72* promotor, whereas numbered gray boxes represent exons not encoded under the *Wdr72* promotor. Black arrows denote primer locations used for genotyping. Green triangles, *frt* sites; Red triangles, *loxP* sites; (B) PCR genotyping of isolated mouse DNA from *Wdr72*$^{+/+}$, *Wdr72*$^{+/-}$, and *Wdr72*$^{-/-}$ tail biopsies. Amplicon sizes of *Wdr72*$^{+}$ allele, 520 bp; and *Wdr72*$^{-}$ allele, 633 bp. (C) Representative photographs of 6-week-old male mandibular incisors (left panels, buccal view) and molars (right panels, lingual view) after soft tissue removal. *Wdr72*$^{-/-}$ enamel was lost from the intact dentin surface when teeth erupted into the oral cavity. *Wdr72*$^{-/-}$ enamel also appeared opaque and stained as compared to the translucent *Wdr72*$^{+/+}$ enamel. (D) Quantitative real-time PCR (qPCR) of micro-dissected secretory and maturation-stage ameloblasts. Wdr72 transcript is successfully knocked out in *Wdr72*$^{-/-}$ mice and is significantly up-regulated from secretory to maturation stages in *Wdr72*$^{+/+}$ amelo-blasts (n=3, $P < 0.05$). Error bars represent ± SD about the mean.

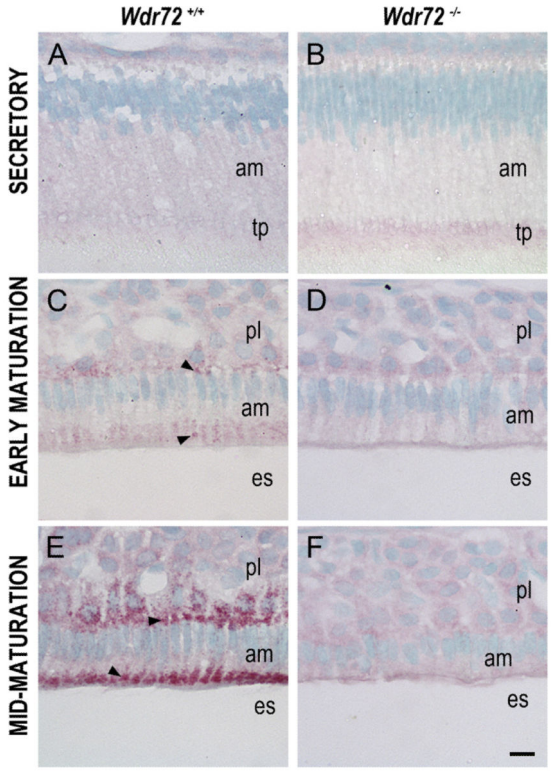

Fig. 4. WDR72 immunolocalizes to vesicle-like puncta in Wdr72$^{+/+}$ maturation-stage ameloblasts and shows protein-level knockout in Wdr72$^{-/-}$ mice

Representative sagittal sections of P10 male *Wdr72*$^{+/+}$ and *Wdr72*$^{-/-}$ mandibles immunostained with a polyclonal rabbit antibody to WDR72 peptide. (A) In *Wdr72*$^{+/+}$ mice, immunoreactivity (red) was diffusely positive in secretory ameloblasts and increased upon entry into the maturation stage (C, E), immunolocalizing to vesicle-like structures at the basal and apical ends (arrowheads). (B, D, F) Slight non-specific background immunoreactivity was present in *Wdr72*$^{-/-}$ ameloblasts. am, ameloblast; es, enamel space; pl, papillary layer; tp, Tomes' process. Scale bar, 10 μm.

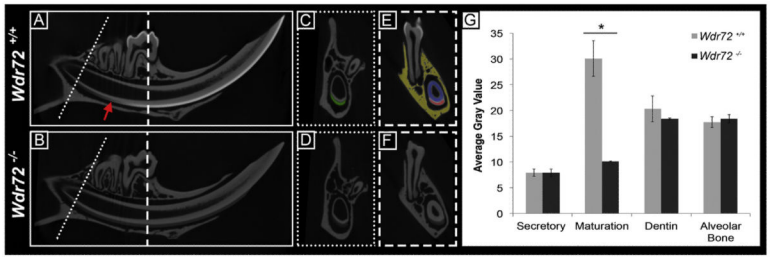

Fig. 5. Hypomineralized enamel phenotype in Wdr72$^{-/-}$ mice occurs at the onset of maturation stage

Representative sagittal (A, B) and cross sectional (C–F) microCT images of Wdr72$^{+/+}$ and Wdr72$^{-/-}$ 6-week-old male mandibles. In the continuously growing incisor, Wdr72$^{+/+}$ enamel mineralization increased at the onset of maturation stage to form an enamel layer of increasing relative intensity (A), which remained radiolucent in the *Wdr72*$^{-/-}$ mice (B). Red arrow marks transition stage. Similar relative intensity comparisons between the *Wdr72*$^{+/+}$ and *Wdr72*$^{-/-}$ enamel were observed in fully formed molars (E, F). Dotted and dashed lines mark the sites along the continuously growing incisor where coronal planes were taken at secretory stage (C, D) and maturation (E, F) stages of enamel, respectively. Dentin and alveolar bone showed no differences (A–D). Green, red, blue, and yellow shading overlays on the *Wdr72*$^{+/+}$ cross-section panels (C & E) represent the regions of interest that were used to quantify the average gray values seen in the bar graph; green, incisor enamel at secretory stage; red, incisor enamel at maturation stage; blue, dentin; yellow, alveolar bone. Quantification of these observations is depicted in the graph to the right (G). Error bars represent ± SD about the mean (n=3). Paired student t-tests between *Wdr72*$^{+/+}$ and *Wdr72*$^{-/-}$ average gray scale values with a threshold for P-values at <0.05. (For interpretation of the references to color in this figure legend, the reader is referred to the web version of this article.)

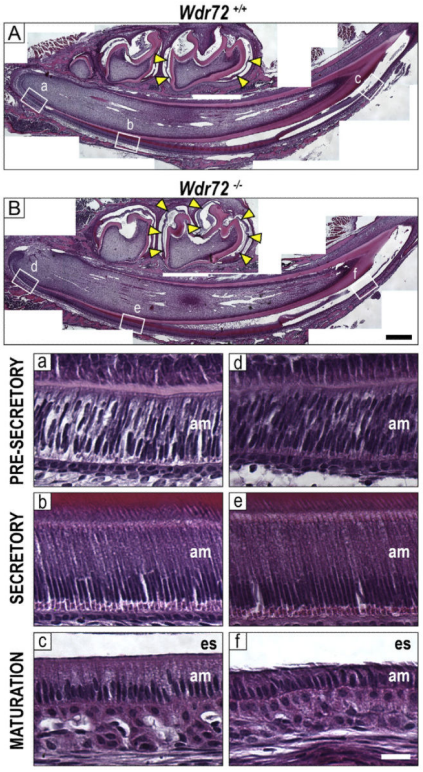

Fig. 6. Enamel matrix and ameloblasts display maturation-stage specific phenotypes in Wdr72$^{-/-}$ mice

Representative sagittal sections of Wdr72$^{+/+}$ (A) and *Wdr72*$^{-/-}$ (B) P10 male mandibles stained with hematoxylin and eosin. Unerupted first molars are at maturation stage, showing a lack of organic material (yellow arrows) in the enamel space of the *Wdr72*$^{+/+}$ mice but retention in the *Wdr72*$^{-/-}$. Lettered white boxes correspond to enlarged images below. Black scale bar, 400 μm. Bottom panels show *Wdr72*$^{+/+}$ (a–c) and *Wdr72*$^{-/-}$ (d–f) ameloblasts at different stages of differentiation, showing the spectrum of enamel development along the continuously growing incisor. During maturation stage, *Wdr72*$^{-/-}$ ameloblasts (f) are shorter in height compared to those of *Wdr72*$^{+/+}$ mice (c), while earlier stages appear to have morphologically normal ameloblasts. am, ameloblasts; es, enamel space. White scale bar, 20 μm. (For interpretation of the references to color in this figure, the reader is referred to the web version of this article.)

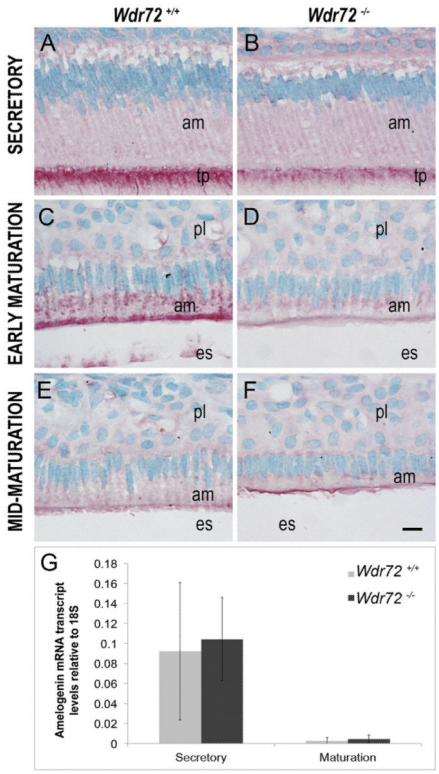

Fig. 7. Wdr72$^{-/-}$ ameloblast cells have decreased intracellular amelogenin proteins with no change in transcript levels

Representative images of ameloblasts from P10 male *Wdr72*$^{+/+}$ and *Wdr72*$^{-/-}$ mice immunostained with amelogenin antibody (red) and counterstained with methyl green. Amelogenin is immunoreactive in secretory ameloblasts at the Tomes' processes (A, B) and in early maturation-stage ameloblasts at the center and apical regions in small puncta (C, D), but was more reactive in *Wdr72*$^{+/+}$ than *Wdr72*$^{-/-}$ mice. As enamel formation progressed to mid-maturation, intracellular amelogenin immunostaining was absent in both *Wdr72*$^{+/+}$ (E) and *Wdr72*$^{-/-}$ (F) ameloblasts. am, ameloblast; es, enamel space; pl, papillary layer. Scale bar, 10 μm. (G) Relative amelogenin mRNA expression in microdissected enamel epithelia from 6-week-old male mice at secretory and maturation stages, showing no significant differences between *Wdr72*$^{+/+}$ and *Wdr72*$^{-/-}$ mice at either secretory ($P = 0.81$) or maturation stages (P = 0.53). Gene copy numbers are relative to 18S. Error bars represent ± SD about the mean (n = 3). (For interpretation of the references to color in this figure legend, the reader is referred to the web version of this article.)

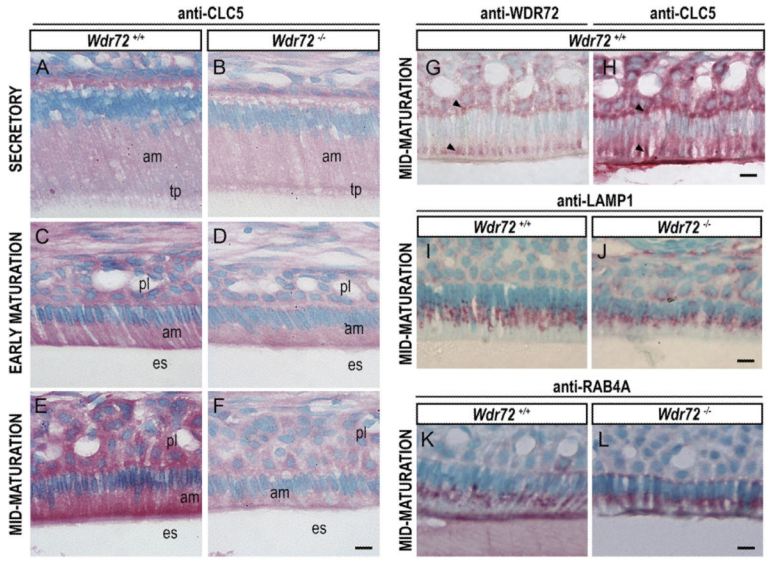

Fig. 8. Immunolocalization of vesicle markers in Wdr72$^{+/+}$ and Wdr72$^{-/-}$ ameloblasts

Immunostaining of CLC5 in *Wdr72*$^{+/+}$ and *Wdr72*$^{-/-}$ ameloblasts (A–F) showed that CLC5 is decreased in maturation-stage ameloblasts of *Wdr72*$^{-/-}$ mice as compared to *Wdr72*$^{+/+}$. Serial sections of *Wdr72*$^{+/+}$ enamel organs at maturation stage showed WDR72 and CLC5 both immunolocalizing in similar patterns at apical and basal regions of the ameloblasts, as well as the papillary layer (G & H, arrowheads). Further immunostaining of LAMP1 (I, J) and RAB4A (K, L) showed no differences between *Wdr72*$^{+/+}$ and *Wdr72*$^{-/-}$ maturation-stage ameloblasts. am, ameloblast; es, enamel space; pl, papillary layer; tp, Tomes' process. Scale bars, 10 μm. (For interpretation of the references to color in this figure legend, the reader is referred to the web version of this article.)